Using a case-study approach to improve the Madden-Julian oscillation in the Hadley Centre model

Article

Published Version

Klingaman, N. ORCID: https://orcid.org/0000-0002-2927-9303 and Woolnough, S. ORCID: https://orcid.org/0000-0003-0500-8514

It is advisable to refer to the publisher's version if you intend to cite from the work. See Guidance on citing.

www.reading.ac.uk/centaur
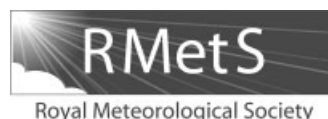
Using a case-study approach to improve the Madden–Julian oscillation in the Hadley Centre model[†]

N. P. Klingaman* and S. J. Woolnough

National Centre for Atmospheric Science–Climate and Department of Meteorology, University of Reading, UK

*Correspondence to: N. P. Klingaman, Department of Meteorology, University of Reading, PO Box 243, Reading, Berkshire, RG6 6BB, UK. E-mail: n.p.klingaman@reading.ac.uk

In its default configuration, the Hadley Centre climate model (GA2.0) simulates roughly one-half the observed level of Madden–Julian oscillation activity, with MJO events often lasting fewer than 7 days.

We use initialized, climate-resolution hindcasts to examine the sensitivity of the GA2.0 MJO to a range of changes in subgrid parametrizations and model configurations. All 22 changes are tested for two cases during the Years of Tropical Convection. Improved skill comes only from (i) disabling vertical momentum transport by convection and (ii) increasing mixing entrainment and detrainment for deep and mid-level convection. These changes are subsequently tested in a further 14 hindcast cases; only (ii) consistently improves MJO skill, from 12 to 22 days. In a 20 year integration, (ii) produces near-observed levels of MJO activity but propagation through the Maritime Continent remains weak.

With default settings, GA2.0 produces precipitation too readily, even in anomalously dry columns. Implementing (ii) decreases the efficiency of convection, permitting instability to build during the suppressed MJO phase and producing a more favourable environment for the active phase. The distribution of daily rain rates is more consistent with satellite data; default entrainment produces $6–12 \, \text{mm} \, \text{day}^{-1}$ too frequently. These results are consistent with recent studies showing that greater sensitivity of convection to moisture improves the representation of the MJO.

Key Words: Madden–Julian oscillation; convection; entrainment; hindcasts; subseasonal variability

Received 8 April 2013; Revised 21 November 2013; Accepted 2 December 2013; Published online in Wiley Online Library

1. Introduction

1.1. The Madden–Julian oscillation

The Madden–Julian oscillation (MJO: Madden and Julian, 1971, 1972) is the dominant mode of subseasonal variability in tropical convection. Although the temporal distribution of MJO events is irregular, the oscillation typically has a period of 30–70 days. Active phases of the MJO consist of an envelope of intense, deep convection that often occurs first in the Indian Ocean before propagating east through the Maritime Continent and into the West Pacific. Clear skies and light winds characterize the MJO suppressed phase, which precedes and follows the active phase. During Northern Hemisphere summer, MJO active and suppressed events propagate north as well as east, influencing the Indian and southeast Asian monsoons (Lawrence and Webster, 2002; Fu and Wang, 2004). The MJO also modulates the African

(Lavender and Matthews, 2009; Alaka and Maloney, 2012) and Australian (Hendon and Liebmann, 1990; Wheeler *et al.*, 2009) monsoons. MJO phase and intensity are used to predict tropical cyclogenesis in the Atlantic, Pacific and Indian Oceans (Leroy and Wheeler, 2008; Camargo *et al.*, 2009), a signal that also appears in some numerical weather prediction (NWP) systems (Vitart, 2009; Belanger *et al.*, 2010; Gall and Ginis, 2011). Through its teleconnections to modes of extratropical variability such as the North Atlantic Oscillation (Cassou, 2008), the MJO provides a key source of weekly and monthly predictability globally. Zhang (2005) provides a more detailed description of the MJO, its life cycle and its teleconnections.

1.2. Modelling the MJO

General circulation models (GCMs) used for NWP, seasonal forecasting and climate simulations often struggle to represent the amplitude, propagation and period of the MJO, as well as its tropical and extratropical teleconnections (Slingo *et al.*, 1996; Waliser *et al.*, 2003; Lin *et al.*, 2006; Kim *et al.*, 2009). Numerous

---

[†]The copyright line for this article was changed on 27 February 2014 after original online publication.

studies have presented the sensitivities of the simulated MJO in one or several models to variations in model configurations (Maloney and Hartmann, 2001). Taking the UK Met Office Hadley Centre model as an example, research has shown that the MJO may be improved by refining the atmospheric vertical resolution (Inness *et al.*, 2001), reducing errors in mean tropical sea-surface temperatures (SSTs) and circulation (Inness *et al.*, 2003), prescribing daily instead of monthly observed SSTs (Klingaman *et al.*, 2008) and improving the representation of air–sea interactions by including the diurnal cycle of surface fluxes and SSTs (Bernie *et al.*, 2008; Klingaman *et al.*, 2011).

Some of these sensitivities have been reproduced in other GCMs. For instance, Woolnough *et al.* (2007) demonstrated that well-resolved atmosphere–ocean coupling improved MJO prediction in the European Centre for Medium-Range Weather Forecasting (ECMWF) Integrated Forecasting System (IFS). In other models, however, ocean coupling had little effect on the simulated MJO (Hendon, 2000; Small *et al.*, 2011). The dependence of the simulated MJO on changes in physical parametrizations or model configurations (e.g. coupling) likely itself depends on the existing level of MJO activity in the model, mean-state biases, the model formulation and the presence of compensating errors.

Recent studies have demonstrated that increasing the sensitivity of parametrized convection to variability in atmospheric moisture improved tropical subseasonal variability, including the MJO (Bechtold *et al.*, 2008; Hannah and Maloney, 2011; Hirons *et al.*, 2012b). Bechtold *et al.* (2008) showed that an update to the IFS considerably improved MJO forecast skill, with the model able to maintain observed MJO amplitude for up to four weeks. Through a series of hindcast experiments, Hirons *et al.* (2012a) identified that the greater skill resulted primarily from reformulating the entrainment rate for 'organized' convection to depend on mid-tropospheric relative humidity rather than on local moisture convergence. Hirons *et al.* (2012b) confirmed that this change reduced the frequency of erroneous deep convection in dry columns, allowing stronger positive moisture anomalies to develop during suppressed MJO conditions and permitting a smooth transition from shallow to deep convection during the active phase. This transition was also shown to be critical for representing the observed MJO amplitude and propagation in the Geophysical Fluid Dynamics Laboratory Atmospheric Model (Benedict and Maloney, 2013). The authors constrained the formation of deep convection by altering the convective trigger and closure, which improved the MJO but worsened tropical mean-state biases. Similarly, Hannah and Maloney (2011) found that either increasing the minimum entrainment rate or the evaporation of falling hydrometeors –both of which heighten the sensitivity of convection to environmental moisture –resulted in better spatial coherence of intraseasonal convection in the Community Atmospheric Model. Satellite and *in situ* observations have confirmed the strong sensitivity of precipitation to column water vapour (Holloway and Neelin, 2009), as well as the transition from shallow to deep convection during the MJO active phase (Del Genio *et al.*, 2012), motivating efforts to improve these processes in GCMs.

1.3. Motivation

A recent development version of the UK Met Office Hadley Centre Global Environmental Model (HadGEM3 GA2.0, hereafter 'GA2.0'; section 2.1) produces roughly one-half of the observed MJO activity (Figure 1). We diagnose overall 'MJO activity' in observations and the 20 year GA2.0 control simulation ('CTL-20yr'; section 5.1) as the fraction of days when the amplitude of the real-time multivariate MJO (RMM: Wheeler and Hendon, 2004) indices is greater than 1. GA2.0 data are projected on to the observed empirical orthogonal function (EOF) patterns, using the method described in section 2.2.

In observations (1975–2012), the MJO spends 7–8% of days outside the RMM unit circle in each phase (Figure 1(a), coloured wedges) for a total of 62% of days outside ('strong MJO') and 38% of days inside the circle ('weak MJO'). The situation is reversed in CTL-20yr: only 33% of days have strong activity (Figure 1(b)). Other diagnostics of MJO activity, including those recommended by the CLIVAR Madden–Julian Oscillation Working Group (2009), confirm the weak MJO in CTL-20yr. We show an example of such a diagnostic, the wavenumber–frequency spectra of $15°S–15°N$ averaged 850 hPa zonal wind, in Figure 1(c) and (d) for observations and CTL-20yr, respectively. The mean and first three harmonics of the annual cycle are removed prior to computing the power spectra, as suggested by the CLIVAR Madden–Julian Oscillation Working Group (2009). Whereas the observations show a peak at eastward wavenumbers 1–3 and periods of 30–50 days, CTL-20yr has very weak power at subseasonal periods; most of the eastward power in CTL-20yr lies at much longer (100–150 day) periods. The diagnostics in Figure 1(a) and (b) provide an accurate, 'one-look' picture of the representation of the MJO in a climate simulation.

When CTL-20yr produces an MJO, it is often unable to maintain it for more than a few days, as demonstrated by lag composites of strong activity in each phase (Figure 1(e) and (f)). This is confirmed by the day+1 transition probabilities shown for each phase in Figure 1(a) and (b). CTL-20yr has MJO 'decay' rates –the probability of a strong MJO moving inside the unit circle on the next day - 67–144% greater than observations.

Improving climate-model biases, whether in the mean state or in variability, is often a frustrating, computationally expensive and time-consuming process. This is partly due to a perceived need for multi-annual or decadal simulations to detect the signal of the imposed changes above the noise of climate variability. Yet systematic errors in climate simulations often occur and sometimes saturate within the first few days or weeks of initialized forecasts (Martin *et al.*, 2010). It is still often difficult to trace errors to particular subgrid-scale parametrization settings, but the computational efficiency of subseasonal, initialized hindcasts permits a wide range of parametrization changes to be tested under a broad set of initial conditions. Initializing from model analyses generated from modern data-assimilation systems minimizes initial-condition error, allowing a more confident attribution of biases to errors in model physics rather than large-scale dynamics.

To examine the sensitivity of the GA2.0 MJO to parametrization and model-configuration changes, we use a set of initialized, climate-resolution hindcasts of cases of strong MJO activity over the past 10 years. Section 3 describes the results of a wide range of changes tested for two cases during the Years of Tropical Convection (YoTC: Waliser *et al.*, 2012). In section 4, results of a more extensive set of hindcast experiments are described, using the two changes that were beneficial in YoTC cases. Only one change resulted in improved model performance for most hindcasts; in section 5 this change is applied to a 20 year GA2.0 integration and compared against CTL-20yr.

2. Model and data

2.1. The HadGEM3 atmospheric model

All simulations are performed with atmosphere-only configurations of HadGEM3. Because HadGEM3 is under development, the Met Office designates particular fixed scientific configurations as 'Global Atmosphere' versions (Walters *et al.*, 2011). In this study, we use the Global Atmosphere version 2 configuration (GA2.0: Hewitt *et al.*, 2011; Arribas *et al.*, 2011). The model resolution is $1.875°$ longitude $\times 1.25°$ latitude (N96) with 85 vertical points, 50 of which are within the tropical troposphere (18 km), and a rigid model lid at 85 km. This is the typical resolution for climate-length
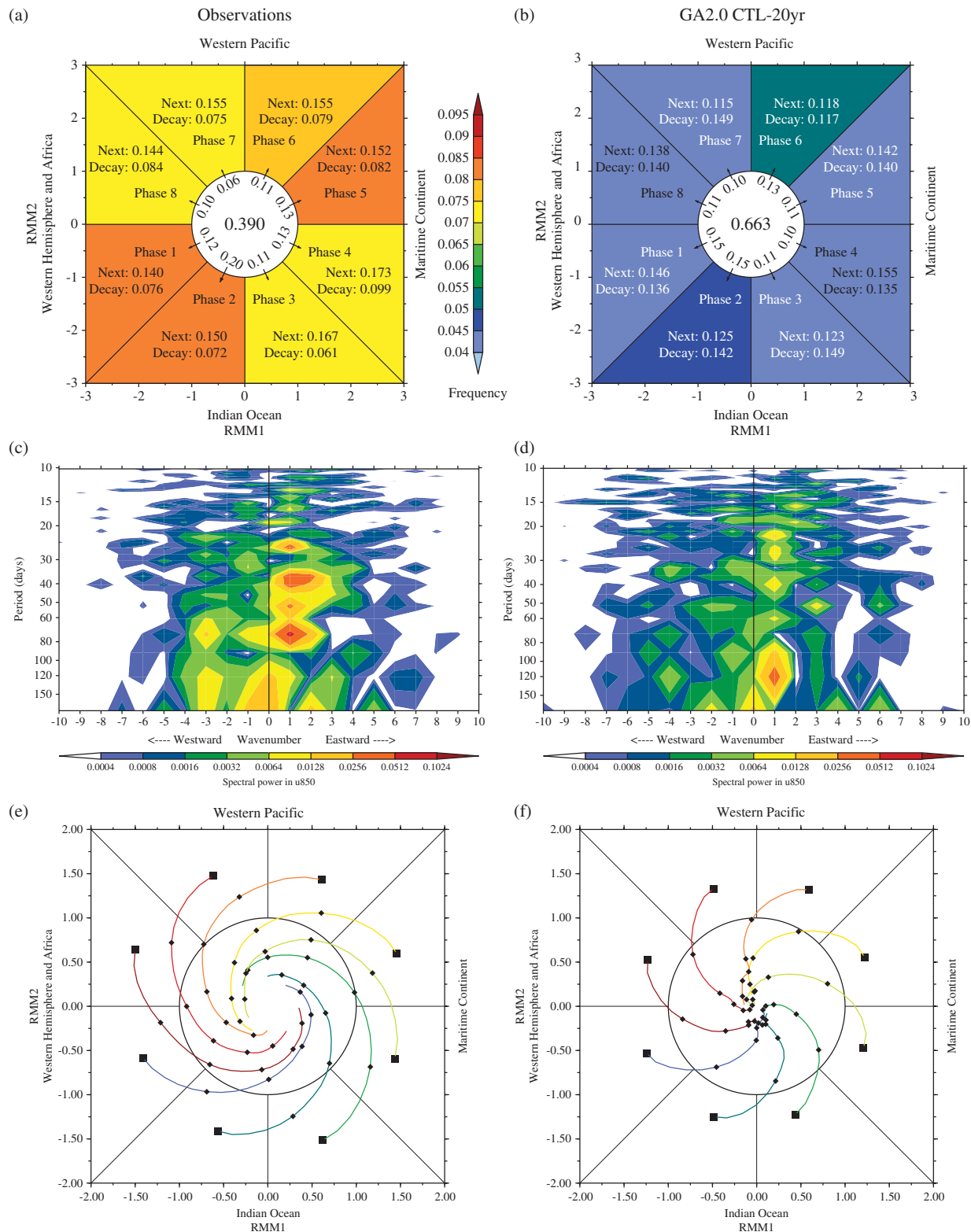
ⓒ 2013 The Authors. *Quarterly Journal of the Royal Meteorological Society* published by John Wiley & Sons Ltd on behalf of the Royal Meteorological Society.

Q. J. R. Meteorol. Soc. (2014)

Figure 1. In panels (a) and (b), the coloured octants show the daily frequency of occurrence of strong MJO activity (amplitude ≥ 1) in each phase, relative to all days. For each phase, the decimal fractions are probabilities that, on the day following strong activity in that phase, the MJO transitions to the next (anticlockwise) phase ('Next') or moves into the unit circle ('Decay', i.e. an amplitude < 1). The frequency of weak MJO activity is given inside the unit circle. The values next to the arrows crossing the unit circle show the relative probabilities of MJO genesis into each phase. Panels (c) and (d) show wavenumber–frequency power spectra of $15°S-15°N$ averaged 850 hPa zonal wind, using (c) NCEP–NCAR Reanalysis winds and (d) GA2.0 CTL-20yr simulation data. The mean and first three harmonics of the annual cycle have been removed prior to computing the power spectra. Panels (e) and (f) show lag composites of strong MJO activity in each phase, with dots spaced every 5 days. Panels (a) and (e) are constructed using RMM indices from NOAA OLR and NCEP–NCAR reanalysis winds for 1975–2012; panels (b) and (f) are constructed using HadGEM3 GA2.0 CTL-20yr simulation data, projected on to the observed Wheeler and Hendon (2004) EOFs.

simulations. Full details of the model physics can be found in Arribas *et al.* (2011) and Walters *et al.* (2011); the latter describes GA2.0 as well as a more recent configuration (GA3.0). A summary of the convection parametrization is provided below, however, as that scheme is particularly important to the results of this study.

Convection in HadGEM3 is parametrized using a heavily altered form of the Gregory and Rowntree (1990) scheme. Modifications include representations of downdraughts (Gregory and Allen, 1991), separate formulations of vertical convective momentum transport (CMT) for diagnosed shallow (Grant and Brown, 1999), mid-level (Gregory *et al.*, 1997) and deep (Stratton

et al., 2009) convection and a closure based on convectively available potential energy (Fritsch and Chappell, 1980). For diagnosed deep and mid-level convection, an ascending plume entrains environmental air at a rate ϵ at each vertical grid point z by

$$\epsilon(z) = 4.5F\frac{p(z)\rho(z)g(z)}{p_*^2}, \qquad (1)$$

where p and ρ are the pressure and density, g is gravity, p_* is the surface pressure and F is a user-modifiable scaling factor with a default value of 0.9. Note that F does not vary with height; changing F, as in this study, scales the entrainment rate equally at all heights. Detrainment of air from diagnosed deep convective plumes is treated with a combination of mixing detrainment (δ_m) as a parcel ascends, which depends upon ϵ and inversely upon the environmental relative humidity, and forced detrainment (δ_f) due to the loss of buoyancy from the plume (Derbyshire et al., 2011). The maximum closure time-scale is a user-modifiable parameter and is often varied with horizontal resolution, but is reduced automatically in rare cases of exceptionally strong ascent (Walters et al., 2011).

2.2. Methods and data

For all GA2.0 hindcasts, the RMM indices were computed using the method described in Gottschalck et al. (2010) for NWP models. Since the hindcasts were initialized from ECMWF operational analyses (section 3.1), the means of the previous $121 - t$ days of those analyses were removed from forecast day t of each simulation before projecting on to the observed EOF structures from Wheeler and Hendon (2004). The model RMM indices are compared against 'observed' indices constructed by the same method, using outgoing long-wave radiation (OLR) data from the National Oceanic and Atmospheric Administration satellite-derived dataset and 850 hPa and 200 hPa zonal winds (U850 and U200, respectively) from the ECMWF analyses.

The observed RMM indices for 1975–2012 used in Figure 1 were obtained from http://www.cawcr.gov.au/staff/mwheeler/maproom/RMM. For the GA2.0 20 year climate integrations, the RMM indices were computed by projecting the model data on to the Wheeler and Hendon (2004) EOFs using the method described in that study.

GA2.0 precipitation is compared against satellite-derived analyses from the Tropical Rainfall Measuring Mission (TRMM) 3B42, version 6A (Kummerow et al., 1998). Pressure-level model fields are compared against 6 hourly ECMWF ERA-Interim (Dee et al., 2011) reanalysis data, converted to daily-mean values. When comparing grid-point fields, all datasets were interpolated on to the GA2.0 horizontal grid using an area-weighted linear method, prior to any other processing.

3. Hindcasts of YoTC cases

3.1. Experiment design

GA2.0 hindcasts were conducted of two strong MJO events –starting on 10 October 2008 ('Oct08') and 6 April 2009 ('Apr09') –during YoTC. The latter of these was also simulated by the Cascade project at higher horizontal resolutions (40–1.5 km: Holloway et al., 2013). For each event, a control hindcast was performed, along with 21 perturbation experiments making single changes to either a model parameter setting or the SST boundary condition. The changes were selected to span a range of likely causes of the deficient MJO seen in both climate (Figure 1) simulations and the short-range, initialized Cascade simulations. The perturbations comprised the following.

- Changing from fixed SSTs from the ECMWF analysis to fixed SSTs from the Met Office Operational SST and sea-Ice Analysis (OSTIA: Donlon et al., 2012) product.
- Using daily, time-varying OSTIA SSTs, based on previous results showing the importance of high-frequency SST variations for simulating subseasonal convection (Klingaman et al., 2008).
- Increasing and decreasing F (Eq. (1)) by 50% for mid-level and deep convection. This increases or decreases the rates of mixing entrainment (ϵ) and mixing detrainment (δ_m).
- Increasing and decreasing δ_m for mid-level and deep convection by 50%, while holding ϵ constant.
- Increasing and decreasing ϵ for mid-level and deep convection by 50%, while holding δ_m constant.
- Increasing δ_f by 100% and decreasing it by 50% (i.e. increasing or decreasing the sensitivity to buoyancy loss).
- Increasing the maximum convective closure time-scale by 100% and decreasing it by 50%; the default value is 5400 s (90 min).
- Increasing and decreasing the threshold vertical velocity (ω) for automatically reducing the closure time-scale by 50%; the default value is 0.3 m s^{-1}.
- Changing the trigger variable for reducing the closure time-scale from ω to relative humidity.
- Disabling CMT for deep and mid-level convection, separately and together.
- Disabling the prognostic cloud scheme (PC2: Wilson et al., 2008).
- Disabling the 'coastal tiling' scheme for fractional land coverage of coastal points that blends land and ocean surface fluxes.
- Reducing the fall velocities of rain droplets to increase drizzle evaporation and moisten the mid-troposphere by using the Abel and Shipway (2007) parametrization.

In addition to these 22 integrations for each event, 15 others were run with combinations of the above changes. For brevity these are not listed; the most important combination is a 50% increase in F and switching off the CMT for deep and mid-level convection, discussed below. All hindcasts were initialized from 0000 UTC (0Z) ECMWF analyses.

3.2. Results

For both cases, the CTL hindcasts damp the MJO amplitude immediately, losing the signal completely within a few days, whereas the observed amplitude grows (Figure 2). The CTL hindcasts also fail to propagate the anomalous convection east; the trace for CTL Apr09 moves 'backwards' into Phase 1 and Phase 8 after losing amplitude. The behaviour in these initialized simulations is similar to that in CTL-20yr (Figure 1): GA2.0 is unable to maintain or propagate anomalous subseasonal convection.

Of the perturbation hindcasts, only the experiments in which F was increased by 50% ('1.5F'), CMT was disabled for deep and mid-level convection ('NoCMT') and the changes were applied together ('1.5F+NoCMT') showed improvements over CTL (Figure 2). Two other experiments, in which the maximum closure time-scale was halved ('0.5*time-scale') and the coastal tiling scheme was disabled ('No tiling'), are shown in Figure 2 as examples of experiments that had little impact on the simulated MJO. For Oct08 and Apr09, NoCMT strengthens RMM amplitude initially and produces propagation from Phase 2 to 3 within the first days of the hindcast. After this, however, amplitude in NoCMT decays as in CTL. 1.5F generates stronger amplitudes throughout the hindcasts, as well as counterclockwise movement around phase space, equivalent to eastward propagation, similar to observations. 1.5F overestimates (underestimates) amplitude over the first 10 days of Oct08 (Apr09). 1.5F+NoCMT reduces the
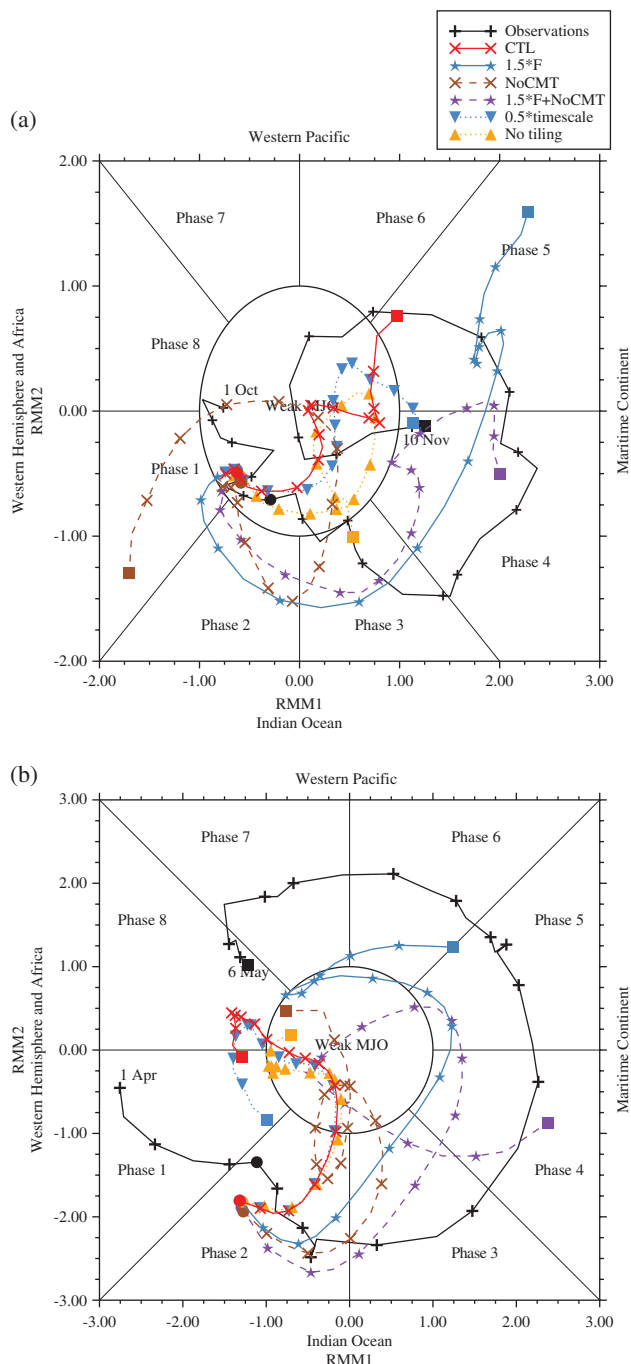
Figure 2. For (a) Oct08 and (b) Apr09 cases, time series of RMM indices from observations (black line) and the hindcast sets shown in the key at the top right (other colours). Day 1 (30) is marked with a circle (square); symbols are spaced every 2 days along the traces.

amplitude in Oct08, bringing the model closer to observations, but fails to propagate the active MJO beyond the Maritime Continent (Phase 5). Still, all three experiments show improved RMM forecasts over CTL from days 1–10.

In addition to $1.5F$, which increases ϵ and δ_m, Oct08 and Apr09 hindcasts were performed in which ϵ and δ_m were separately increased by 50% (section 3.1, not shown). The increase to ϵ alone improved skill for both events, but the amplitude of the RMM indices decayed more rapidly than in $1.5F$. Increasing only δ_m produced little change from CTL. Raising ϵ therefore provides most of the greater MJO predictability seen in $1.5F$, but some additional skill comes from increasing δ_m together with ϵ. A proposed mechanism linking higher ϵ and increased MJO performance is discussed in sections 4.2.2 and 6.

To assess the propagation of MJO convection and associated circulation, longitude–time Hövmoller diagrams are constructed

for 5°S–5°N averaged precipitation and $U200$ (Figure 3). TRMM shows an initial westward movement of the strongest precipitation for Oct08 (Figure 3(a)), followed by coherent eastward propagation for Oct08 and Apr09 (Figure 3(k)). The phase speed is faster for Apr09, which also shows a bifurcation of the precipitation band once it crosses the Maritime Continent. CTL shows diffuse precipitation across the Equator, with a prevalence of light and moderate rain rates (2–8 mm day^{-1}) and a lack of < 2 mm day^{-1} rain rates (white contour in Figure 3), with no organization or eastward propagation (Figure 3(b) and (l)). For Oct08, CTL produces westward propagation, consistent with the clockwise movement in RMM phase space (Figure 2(a)). The dominance of light and moderate rain rates and the absence of near-zero precipitation likely indicate that GA2.0 removes positive moisture anomalies from the atmosphere too quickly, without allowing instability to build during the suppressed phase of the MJO. These findings, together with previous research on the sensitivity of convection to environmental moisture (Hannah and Maloney, 2011; Hirons *et al.*, 2012b), prompted the $1.5F$ experiment.

The strong equatorial 200 hPa easterlies in the initial conditions west of the convection (40–55°E) quickly decay in CTL (Figure 3(g) and (q)). This may be because of the lack of a coherent envelope of deep convection to reinforce the easterlies through upper-level divergence, but an overly strong vertical transport of low-level westerly momentum by convection could also be responsible. The latter hypothesis motivated the NoCMT experiment. In NoCMT, GA2.0 maintains the strong $U200$ easterlies for longer than in CTL, with some eastward propagation, particularly in the first 10 days of the hindcasts (Figure 3(h) and (r)). Disabling CMT also strengthened the $U850$ westerlies west of the convection (not shown). There is little change in predicted precipitation, however (Figure 3(c) and (m)). The improved RMM indices for NoCMT in the first few days of the hindcast were found to come mainly from the wind components (not shown). This is not surprising, given that (i) the wind components, rather than OLR, dominate the amplitude and variability of RMM indices (Straub, 2013) and (ii) removing CMT would be expected to influence winds more than OLR. These results suggest that the sharp declines in the upper-level easterlies and low-level westerlies in CTL are due partially to too-strong weakening of the vertical shear by convection.

In $1.5F$ there is improved spatial coherence and propagation of precipitation (Figure 3(d) and (n), respectively). Higher F suppresses the too-frequent light rain rates in CTL, increasing the occurrence of near-zero precipitation, and focuses the convection into the core of the active MJO, enhancing rainfall there. Propagation speeds are similar to observations, particularly during the first 15 days. The $U200$ easterlies (Figure 3(i) and (s)) and $U850$ westerlies (not shown) are stronger in $1.5F$ than in CTL; there is coherent eastward propagation at both levels, likely driven by the stronger, more coherent and propagating enhanced convection. The winds are still weaker than the ECMWF analyses, however. In Apr09 the easterlies are much broader zonally, probably due to the development of a second region of heavy rainfall near 100°E late in the hindcast.

Only in $1.5F+$NoCMT do the $U200$ (Figure 3(j) and (t)) and $U850$ winds reach the intensity of those in ECMWF analyses. Disabling CMT is not necessary to obtain winds that propagate with the convective envelope but, based on the Oct08 and Apr09 cases, including CMT weakens the zonal shear with height too strongly. In $1.5F+$NoCMT, the strength and coherence of convection is reduced after the first 10 days, particularly for Oct08 (Figure 3(e)), relative to $1.5F$ (Figure 3(d)). From only two case studies, however, it is difficult to discern whether this effect is robust.

Based on the Oct08 and Apr09 cases, increasing F in GA2.0 improves the coherence and propagation of enhanced convection while strengthening the suppressed phase by reducing the prevalence of light rain rates in CTL. Disabling CMT amplifies
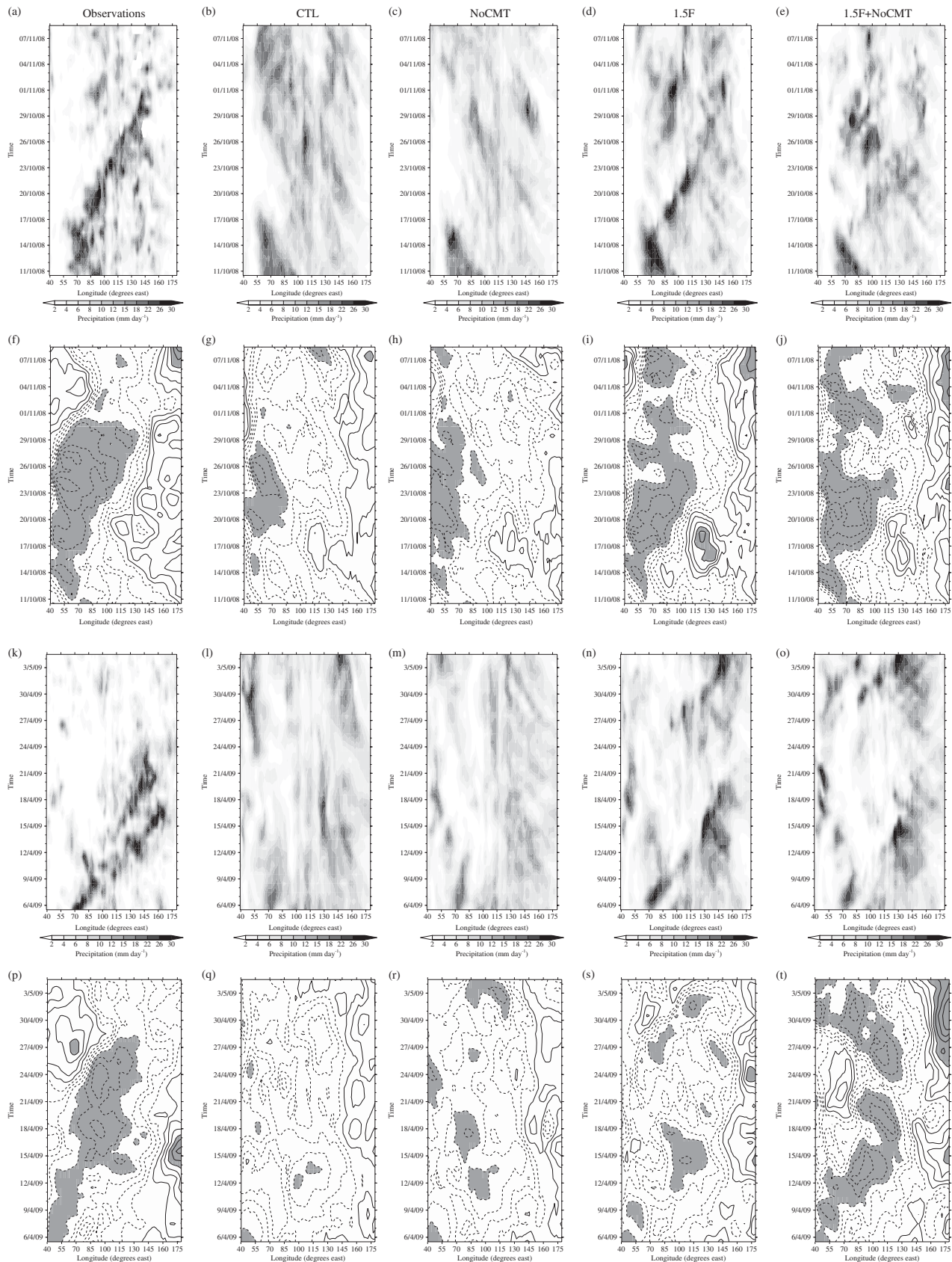
ⓒ 2013 The Authors. *Quarterly Journal of the Royal Meteorological Society* published by John Wiley & Sons Ltd on behalf of the Royal Meteorological Society.

Q. J. R. Meteorol. Soc. (2014)

Figure 3. For (a)−(j) Oct08 and (k)−(t) Apr09 cases, time−longitude Hovmöller diagrams of equatorially averaged (5°S−5°N) ((a)−(e), (k)−(o)) precipitation (mm day^{-1}) and ((f)−(j), (p)−(t)) $U200$ winds (m s^{-1}) for ((a), (k)) TRMM 3B42, ((f), (p)) ECMWF operational analyses and ((b), (g), (l), (q)) CTL, ((c), (h), (m), (r)) NoCMT, ((d), (i), (n), (s)) 1.5F and ((e), (j), (o), (t)) 1.5F+NoCMT hindcasts. The contour interval for $U200$ is 4 m s^{-1} from ± 2 m s^{-1}; negative values are shown with dashed contours; values greater than 14 m s^{-1} or less than -14 m s^{-1} are shaded for emphasis.

the zonal shear with height associated with the envelope of deep convection, which was considerably weaker in CTL than observed, improving the predictability of the RMM wind components. None of the other perturbations listed in section 3.1 produced any notable improvement in skill over CTL.

4. Further hindcast experiments

Based on the results of the Oct08 and Apr09 simulations (section 3.2), the 1.5F, NoCMT and 1.5F+NoCMT perturbations were tested in hindcasts of a set of 14 MJO cases. The selection

ⓒ 2013 The Authors. *Quarterly Journal of the Royal Meteorological Society* published by John Wiley & Sons Ltd on behalf of the Royal Meteorological Society.

Q. J. R. Meteorol. Soc. (2014)

Table 1. Initialization dates for the Day-*n* and Day-*n*+10 hindcast sets.

Day *n* initialization date	Day *n*+10 initialization date
28 September 2000	8 October 2000
13 November 2000	23 November 2000
16 January 2001	26 January 2001
26 April 2002	6 May 2002
5 June 2002	15 June 2002
29 October 2002	8 November 2002
12 December 2003	22 December 2003
18 March 2005	28 March 2005
7 September 2006	17 September 2006
7 December 2007	17 December 2007
26 August 2008	5 September 2008
10 October 2008	20 October 2008
6 April 2009	16 April 2009
4 November 2009	14 November 2009

Figure 4. As in Figure 2, but for composites of (a) Day-*n* and (b) Day-*n*+10 hindcast sets.

of the cases is described in section 4.1; MJO predictability in each hindcast set is analysed in section 4.2.1; the relationship between convection and moisture in CTL and 1.5*F* are examined in section 4.2.2.

4.1. Experiment design

Events in 2000−2009 were selected that met three criteria: (i) the RMM amplitude was >1 in Phase 2 (Indian Ocean) on day *n*; (ii) the amplitude was >1 in Phase 6 (West Pacific) on at least 1 day between *n*+20 and *n*+30; and (iii) the amplitude was >1 in any phase on all days from *n* to *n*+30. Such stringent criteria resulted in the selection of highly similar, strong, propagating MJO events that form a consistent composite. Thirteen events met these criteria, including the Apr09 event. [Oct08 does not meet criterion (i) because the amplitude first became >1 in Phase 3, but meets the other two criteria; it is included as the hindcast data were already available.] Table 1 lists the earliest day *n* meeting all three criteria.

Two 30-day CTL, NoCMT, 1.5*F* and 1.5*F*+NoCMT hindcasts were performed for each case. The first hindcast (the 'Day-*n* hindcasts') was initialized on day *n*. To test that our results were not sensitive to our choice to initialize the model with a strong Phase 2 MJO, a second hindcast was initialized on day *n*+10 (the 'Day-*n*+10 hindcasts': Table 1). These dates have strong MJO events, either Phase 3 or Phase 4. Cases are identified by a three-letter abbreviation for the month in which the Day-*n* hindcasts start, followed by the last two digits of the year. Composites of Day-*n* and Day-*n*+10 hindcasts were constructed by averaging across all 14 cases. For brevity, analysis of the composites is presented in lieu of the individual cases. By construction, the temporal evolution of the observed events is highly similar, which suggests a limited loss of fidelity in considering the composites over the individual cases.

4.2. Results

4.2.1. Predictive skill

As for Oct08 and Apr09, the composite CTL Day-*n* and Day-*n*+10 hindcasts severely damp the amplitude of the MJO a few days after initialization (Figure 4(a) and (b), respectively). NoCMT provides little additional predictability, in contrast to the results for the YoTC cases in which NoCMT maintained the observed amplitude of the RMM indices for several days longer than CTL (Figure 2). To examine the consistency of this behaviour across the hindcast cases, for each 30 day hindcast we compute the bivariate root-mean-squared error (RMSE) of RMM1 and RMM2 against the observed values (Table 2), as in Lin *et al.* (2008), Gottschalck *et al.* (2010) and Rashid *et al.* (2011). Only in a few cases does NoCMT show substantially
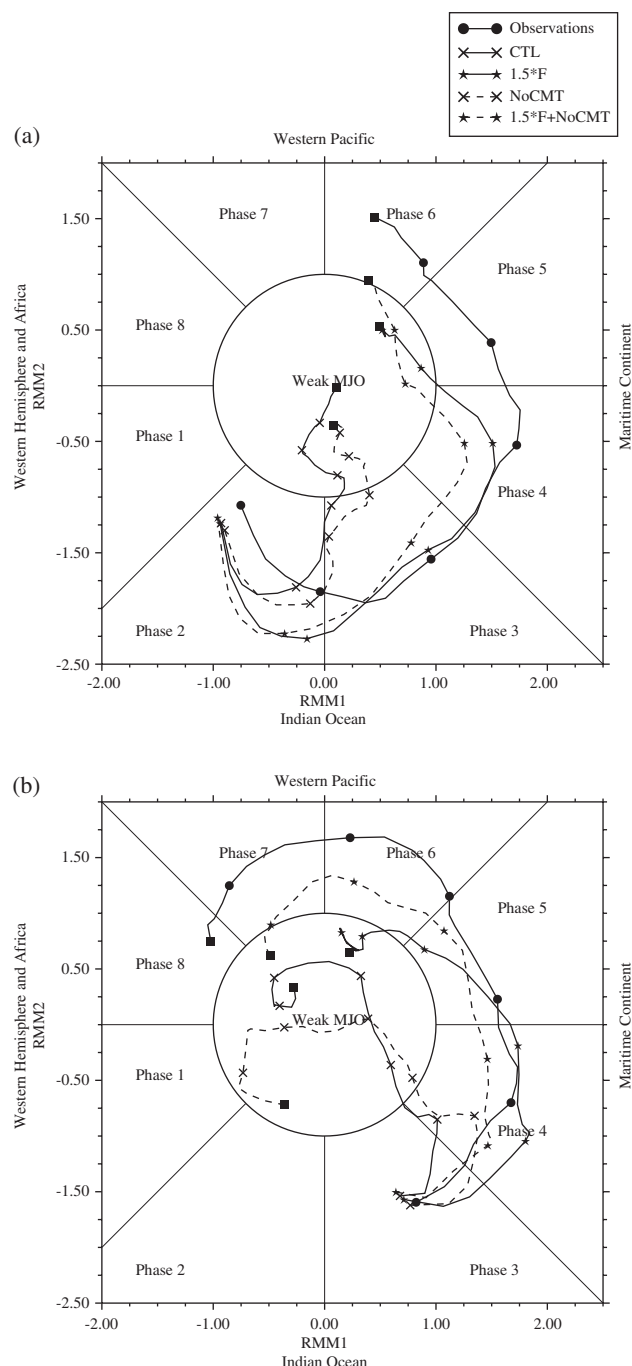
lower RMSE than CTL, notably Jun02 and Oct02 for Day-*n* and Nov00, Apr02, Jun02 and Aug08 for Day-*n*+10. Otherwise, the NoCMT RMSE values are either similar to or greater than the CTL values.

To examine the loss of hindcast skill, the bivariate correlation and RMSE of hindcast RMM1 and RMM2 are computed as against observations as a function of lead time, across all Day-*n* and Day-*n*+10 cases (Figure 5). We also compute the bivariate correlation and RMSE for a persistence forecast, in which the initial observed values of RMM1 and RMM2 are held fixed, against observations. Using a threshold correlation value of 0.6, which will be used for all measures of 'skill' in this study, the CTL and NoCMT hindcasts display 12 days of skill, barely above the 8 days for the persistence forecast. ('Skill' here is strictly limited to the admittedly very small hindcast set employed in this study; further discussion is provided in section 6.) The NoCMT hindcasts have slightly higher correlation and lower RMSE values than CTL over the first few days of the hindcast, after which the

Table 2. For each Day-n (left columns) and Day-$n+10$ (right columns) case, the bivariate RMSE in RMM1 and RMM2 against observations for a persistence forecast ('Persist') and CTL, 1.5F, NoCMT and 1.5F+NoCMT is given. The lowest RMSE for each case is italicized and emphasized.

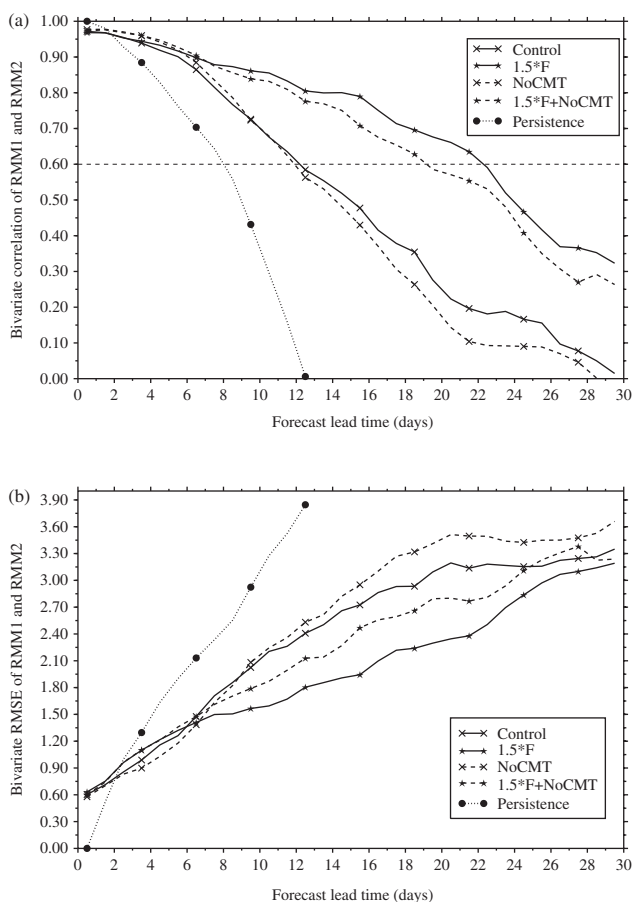| Case	Day-n hindcasts					Day-$n+10$ hindcasts				
	Persist	CTL	1.5F	NoCMT	1.5F+NoCMT	Persist	CTL	1.5F	NoCMT	1.5F+NoCMT
Sep00	2.296	1.763	*1.088*	2.010	1.553	1.294	1.334	*1.046*	1.198	1.160
Nov00	2.113	1.858	*1.390*	1.405	1.773	2.360	2.265	1.328	*1.311*	1.589
Jan01	2.371	2.385	*1.637*	2.545	1.657	3.392	2.512	*2.135*	3.446	2.492
Apr02	2.666	1.584	*1.071*	1.293	1.673	3.844	1.493	1.713	*0.788*	2.290
Jun02	2.951	2.086	1.288	1.335	*1.235*	3.505	2.060	1.522	*1.198*	2.310
Oct02	2.589	2.288	1.533	1.542	*1.433*	2.688	1.933	1.447	2.147	*1.378*
Dec03	2.349	2.368	*1.576*	1.810	1.867	3.263	2.719	*1.746*	2.310	2.091
Mar05	2.865	1.722	*0.611*	1.257	0.817	3.779	1.375	*1.094*	1.976	1.541
Sep06	2.526	1.398	*0.908*	1.361	1.674	2.416	2.114	*1.153*	2.064	1.353
Dec07	2.641	2.388	*1.907*	2.828	1.957	3.595	1.978	*1.850*	2.784	2.114
Aug08	1.990	1.642	*1.263*	2.238	1.431	1.737	1.990	1.902	*1.050*	1.357
Oct08	1.765	1.864	1.243	1.566	*1.203*	2.142	2.014	*1.330*	1.892	1.542
Apr09	3.082	1.934	*1.443*	2.075	2.120	2.589	1.994	*1.002*	2.042	1.878
Nov09	2.197	1.330	1.300	1.343	*0.894*	2.833	2.118	1.142	1.583	*1.034*

Figure 5. Lead-time-dependent bivariate (a) correlation and (b) RMSE in RMM1 and RMM2 against observations for (solid, crosses) CTL, (solid, stars) 1.5F, (dashed, crosses) NoCMT, (dashed, stars) 1.5F+NoCMT and (dotted, circles) a persistence forecast, computed across all Day-n and Day-$n+10$ cases. The persistence forecast traces are truncated when they reaches the edges of the vertical axes.

propagation speeds agree well with observations for the first three weeks of the composite. The 1.5F hindcasts have the lowest RMSE for 18 of 28 cases (Table 2) and 22 days of skill (Figure 5), a considerable improvement over CTL (12 days). The impact of increasing entrainment and detrainment is substantial and repeatable across the Day-n and Day-$n+10$ sets.

Removing CMT at higher F (1.5F+NoCMT) has the same impact as at the control F (NoCMT): a small increase in correlation and decrease in RMSE over the first few days of the hindcast (Figure 5), followed by a decline in skill. For most cases, the RMSE for 1.5F+NoCMT is similar to or greater than that for 1.5F; 1.5F+NoCMT has only 19 days of skill, compared with 22 days for 1.5F.

To ascertain which components of the RMM indices are responsible for the improved correlation and decreased RMSE in 1.5F and 1.5F+NoCMT, bivariate correlations and RMSEs are computed for the contributions of OLR, $U850$ and $U200$ to RMM1 and RMM2 (Figure 6). CTL and NoCMT fail to show any improvement in OLR over persistence (Figure 6(a)), which is consistent with a lack of propagation. Increasing F gives a 4–5 day improvement over persistence, but skill is still limited to less than two weeks. All hindcasts show a sharp drop in the correlation for OLR at day 8–10; the decrease is larger, steeper and somewhat earlier in the CTL and NoCMT hindcasts. There is a small reduction in RMSE for OLR with increased F (Figure 6(b)). The RMSE increases at 8–10 days lead time in all hindcasts, concomitant with the decrease in the correlation. OLR contributes far less to the RMM indices on average than $U850$ or $U200$ (Straub, 2013), explaining the smaller overall RMSEs for OLR than for the wind fields.

Skill in the $U850$ and $U200$ components is considerably greater than for OLR in all hindcasts. The high F hindcast sets have higher correlations and lower RMSEs than CTL and NoCMT, indicating that 1.5F is entirely responsible for improving the circulation. Given the small hindcast set, there is likely no statistically significant difference between the hindcasts with and without CMT at the same F. Correlations are somewhat greater and RMSEs somewhat lower in 1.5F for $U850$ than $U200$ (Figure 6).

The RMM correlation with lead time in GA2.0 is limited first by skill in predicting the RMM OLR components rather than the wind components (i.e. skill in the OLR components declines more quickly with lead time than skill in the wind components). OLR is the best available measure of convection in observations; while OLR is often used as a proxy for convection in models, there is often an imperfect relationship between the strength of OLR anomalies and the strength of convection, as measured by ω or velocity potential. Models often exhibit considerable biases in OLR due to errors in cloud height or optical depth. OLR is likely not the most accurate measure of convective activity in models,
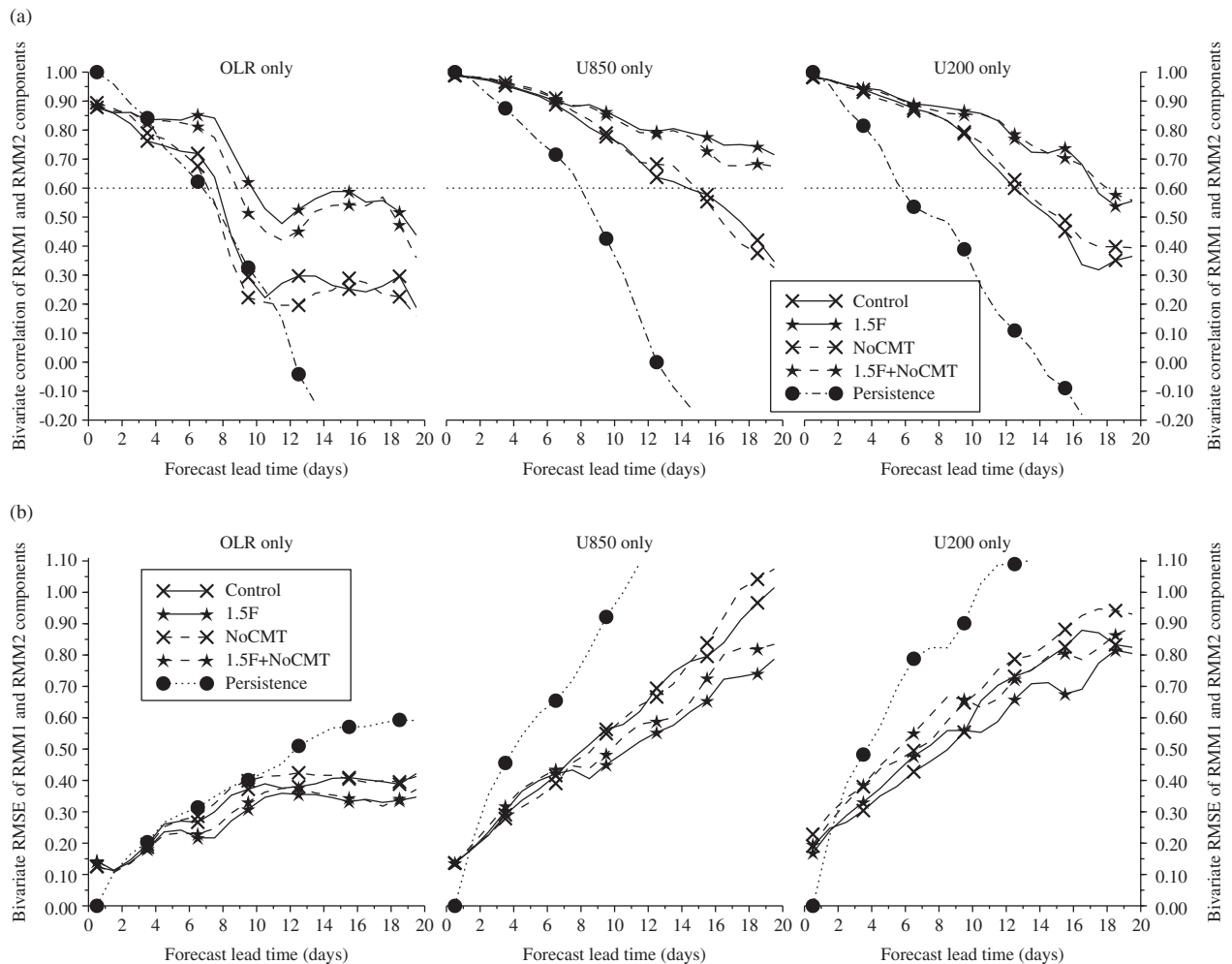
skill declines precipitously, as for the composite RMM traces in Figure 4. While NoCMT improved the $U850$ and $U200$ fields in the Oct08 and Apr09 cases, across the wider hindcast set the impact is negligible.

Increasing F consistently improves the Day-n and Day-$n+10$ hindcasts. The 1.5F Day-n composite propagates from the Indian Ocean into the Maritime Continent, before losing amplitude as it reaches Phase 5 around day 20 (Figure 4(a)). Similarly, the Day-$n+10$ composite propagates through the Maritime Continent and into the West Pacific (Figure 4(b)). The amplitudes and

(a)

(b)

Figure 6. As in Figure 5, but for the bivariate (a) correlation and (b) RMSE with lead time in each component of the RMM1 and RMM2 indices: (left) outgoing long-wave radiation, (centre) 850 hPa zonal wind and (right) 200 hPa zonal wind. The persistence forecast traces are truncated when they reach the edges of the vertical axes.

but it is assessed here because it is a component of the 'real-world' RMM indices. The lower skill in the OLR components may not be due to errors in predicting convection itself, but rather to model OLR biases.

Therefore, 1.5*F* is the sole perturbation of 21 (section 3.1) that considerably and consistently improves the GA2.0 MJO in these hindcasts. This argues that the representation of the MJO in GA2.0 depends upon the sensitivity of parametrized convection to tropospheric moisture, in agreement with recent studies using other GCMs (Hannah and Maloney, 2011; Hirons *et al.*, 2012b). The next section examines that sensitivity further.

4.2.2. Relationships between convection and moisture

Composites across cases of precipitation and column water vapour (CWV) are taken near the initial time, to examine the atmospheric response to the initialized MJO activity in CTL and 1.5*F* before the convection weakens and becomes fragmented in CTL, which happens within 5 days (Figure 4). To avoid model spin-up from the ECMWF analyses, we discard the first 24 h of each simulation. The adjustment is particularly strong in 1.5*F* because the tropical troposphere quickly moistens and precipitation decreases sharply in response to higher *F*. Therefore, we composite on day 3 (Figure 7(a)) as well as on the difference between days 3 and 2 (Figure 7(b)). Since the Day-*n* hindcasts were initialized with strong Phase 2 events, the spatial patterns of convection are highly coherent among the cases; the Day-*n*+10 hindcasts are not included as there is less coherence among these cases. All results discussed below were assessed with a Student's *t*-test, with the null hypothesis that the difference

between CTL and 1.5*F* is zero, and found to be statistically significant at the 5% level.

In CTL and 1.5*F*, the heaviest day 3 precipitation occurs across 65–95°E (Figure 7(a)), with column drying (moistening) in the western (eastern) half of the band relative to day 2 (Figure 7(b)). The moistening is broader and stronger in 1.5*F*, extending through the Maritime Continent into the West Pacific, whereas CTL dries slightly over the Maritime Continent. The greatest differences in CWV between 1.5*F* and CTL occur near 100°E, on the leading edge of the active phase, where precipitation in 1.5*F* sharply decreases relative to CTL, suggesting that maintaining moisture and suppressing precipitation on the eastern edge of the region of active convection may be critical for MJO propagation in this model. The additional moistening in 1.5*F* is concentrated at 900–600 hPa (not shown). There is also roughly a 10% decrease (increase) in precipitation across 60–70°E (80–90°E) in 1.5*F* relative to CTL, suggesting that, by day 3, 1.5*F* has already improved eastward propagation. Composites of ω (not shown) indicate a more intense and zonally extended region of ascent in 1.5*F* relative to CTL, particularly between 85–95°E. There is increased transport of moisture out of the boundary layer in 1.5*F* in the area of active convection, with drying relative to CTL below the boundary-layer top (near 900 hPa) and moistening above it (not shown).

To the east of the MJO active phase, over the Maritime Continent (100–130°E), 1.5*F* has 4–7 mm higher CWV than CTL. Precipitation is considerably reduced in 1.5*F* to 4.2 mm day^{-1}, from 7.6 mm day^{-1} in CTL. There is increased low-level moistening and upper-level drying in 1.5*F* relative to CTL (not shown). This is indicative of convection terminating and
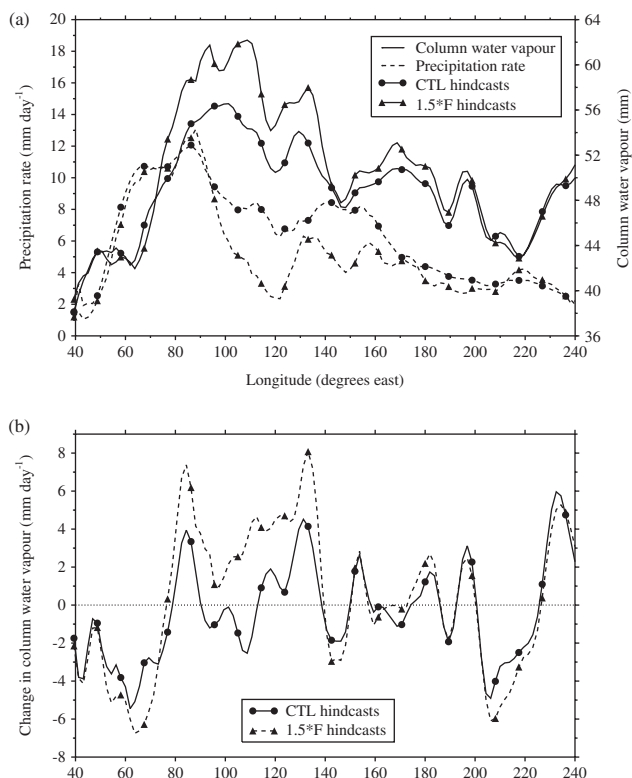
Figure 7. For $10°S–10°N$ averages, (a) composite daily mean precipitation (dashed, left axis) and column water vapour (solid, right axis) on day 3 of the CTL (circles) and $1.5F$ (triangles) Day-n hindcasts and (b) composite difference in daily-mean column water vapour for day 3 minus day 2 of the CTL (solid, circles) and $1.5F$ (triangles) Day-n.

detraining lower in the atmosphere, an expected consequence of increased entrainment and detrainment rates (see section 6). Composites of ω show anomalous column descent in $1.5F$ relative to CTL (not shown). Together, these results suggest an improved representation of the MJO suppressed phase over the Maritime Continent and West Pacific in $1.5F$, pre-conditioning the atmosphere for the impending active phase by sustaining high CWV on through reduced precipitation and increased low- and mid-level detrainment. Our results agree with Kim *et al.* (2014), who found that dry anomalies in the West Pacific (i.e. a stronger suppressed phase) improved propagation through the Maritime Continent. Figure 7(a) clearly demonstrates the reduced precipitation in $1.5F$ in the West Pacific.

To examine the relationship between precipitation and vertical profiles of moisture anomalies, grid-point daily-mean anomalies in specific humidity are composited on grid-point daily-mean rainfall, similar to the analysis performed in Thayer-Calder and Randall (2009), Kim *et al.* (2012) and Xavier (2012). Anomalies are computed from the zonal mean, which is calculated daily using all longitudes; the statistics are accumulated over GA2.0 ocean grid points in a region approximating the Indo-Pacific Warm Pool ($10°S–10°N$, $60°E–180°$). Computing anomalies from a time-varying zonal mean should limit the impact of model drift during the hindcasts (Gottschalck *et al.*, 2010). The mean anomaly in specific humidity is computed for each range of rainfall values (Figure 8). The boundaries of the rainfall ranges are chosen such that TRMM is approximately equally distributed (Figure 8(a), dashed line on right vertical axis). ERA-Interim specific humidity is composited on TRMM rainfall to give an 'observed' estimate. Composites from TRMM/ERA-Interim, CTL (Figure 8(b)) and $1.5F$ (Figure 8(c)) are constructed for all Day-n and Day-$n+10$ cases. Only days 3–30 of each hindcast are used, to prevent influence from the tropospheric moistening during the spin-up of $1.5F$, as discussed above.

In TRMM/ERA-Interim, low-level positive moisture anomalies occur at all but the lightest rain rates. At rates greater than

$1.5\,mm\,day^{-1}$, the entire column is anomalously moist. In the vertical, moisture anomalies peak in the lower troposphere below the freezing level, near 750 hPa. In CTL, light rain occurs in columns that are strongly anomalously dry. At rain rates of $2.5–3.0\,mm\,day^{-1}$, almost the entire column is anomalously dry. Dry anomalies are particularly strong in the mid-troposphere ($400–700$ hPa). The entire column does not become anomalously moist until $6.0\,mm\,day^{-1}$, a considerably higher rain rate than in TRMM/ERA-Interim. This suggests that the convection scheme is triggering too readily in columns with little moisture, removing that moisture as light precipitation and so not allowing moisture anomalies to build.

Increasing F reduces the prevalence of mid-tropospheric dry anomalies associated with light rain rates in CTL. Except for the uppermost troposphere, the column is anomalously moist at $2.5–3.0\,mm\,day^{-1}$. While in CTL most rain rates showed either dry or moist anomalies at all levels, in $1.5F$ light and moderate rain rates show lower- and mid-tropospheric moist anomalies and upper-level dry anomalies. This is more consistent with TRMM/ERA-Interim, although in $1.5F$ such behaviour occurs at somewhat larger rain rates. This suggests that $1.5F$ suppresses the tendency of the convection scheme to trigger in dry environments, permitting more moisture to accumulate in the lower and mid-troposphere, essentially an improved MJO suppressed phase. This agrees with the precipitation Hovmöller diagrams from the YoTC hindcasts (Figure 3), in which CTL produced light rainfall continuously, whereas $1.5F$ showed a region of strong, coherent convection with little precipitation elsewhere, in agreement with TRMM. There are still errors in the precipitation–moisture relationship in $1.5F$: the lightest rain rates are still produced from columns with strong dry anomalies, while heavier precipitation occurs in columns with moisture anomalies that are stronger than ERA-Interim or CTL. Relative to CTL, $1.5F$ not only improves the vertical distribution of moisture anomalies at a given rain rate, but also associates all non-zero rain rates with moister columns (more positive moisture anomalies).

To ensure that the mean moisture anomalies shown in Figure 8 were representative of the behaviour of all grid points in each range of rain rates, the percentage of points with positive moisture anomalies was computed at each pressure level and within each range (not shown). Except in regions with small anomalies ($0.2\,g\,kg^{-1}$ or less), at least 80% of the points agreed with Figure 8 on the sign of the moisture anomaly for TRMM/ERA-Interim and the hindcasts.

CTL also shows a strong preference for $6–16\,mm\,day^{-1}$ rain rates, with relatively less frequent lighter and heavier rainfall relative to TRMM. In $1.5F$, the occurrence of rain rates lighter than $6\,mm\,day^{-1}$ and heavier than $16\,mm\,day^{-1}$ increases considerably with respect to CTL, with a decrease in the 'moderate' range that CTL preferred. This agrees with the analysis of Hovmöller diagrams of precipitation (Figure 3) for the initial two YoTC case studies (section 3.2). Increasing entrainment and detrainment produces a distribution of rain rates closer to TRMM for these events.

5. Climate-length simulations

The hindcast simulations demonstrate that, when GA2.0 is initialized with a strong MJO in the Indian Ocean, $1.5F$ improves the ability of GA2.0 to simulate the intensity and eastward propagation of active convection, likely by altering the relationship between convection and moisture (section 4). The hindcasts do not cover MJO activity in all phases, nor do they test the ability of GA2.0 to generate an MJO when one is not present in the initial conditions. The poor representation of the MJO in a 20 year atmosphere-only simulation (CTL-20yr) was the motivation for this study (section 1.3); the case-study approach was designed to reduce the computational expense of testing sensitivities to many parametrization changes. Having established
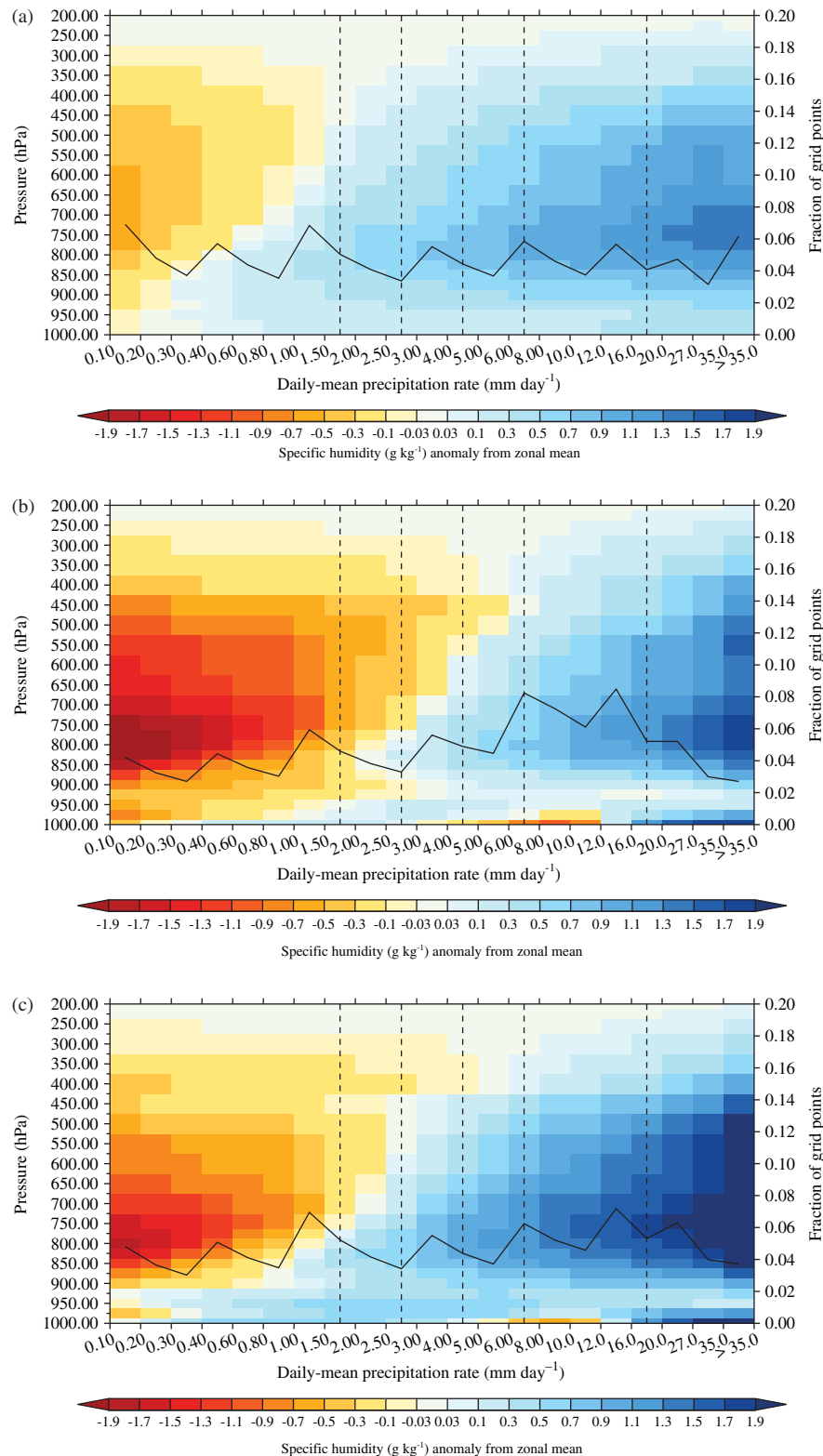
Figure 8. The shading shows anomalies in daily-mean grid-point specific humidity from the zonal mean, composited by daily-mean grid-point precipitation rate, over all Day-n and Day-n+10 cases (days 3–30 only) for (a) ERA-Interim specific humidity and TRMM rainfall, (b) CTL and (c) 1.5F. The solid black line shows the fraction of grid points in each precipitation bin, using the right-hand vertical axis. Statistics are accumulated over GA2.0 ocean points within 10°S–10°N and 60°E–180°; zonal means are computed using all longitudes. Dashed lines are placed at key rain rates to allow easy comparison of the three panels.

1.5F as a key sensitivity in the hindcasts, we implemented 1.5F in a 20 year, atmosphere-only simulation ('1.5F-20yr').

5.1. Experiment design

CTL-20yr and 1.5F-20yr are forced by a repeating climatological (1980–2009) seasonal cycle of SSTs and sea ice, updated daily. Including interannual SST and sea-ice variability produced only small differences in MJO activity (not shown). We

present CTL-20yr and 1.5F-20yr because similar integrations are used in a separate article (Klingaman and Woolnough, 2013) focused on processes controlling the MJO in climate-length simulations.

5.2. Results

Increasing F improves MJO activity in all RMM phases (Figure 9(a)) relative to CTL-20yr (Figure 1(b)), bringing
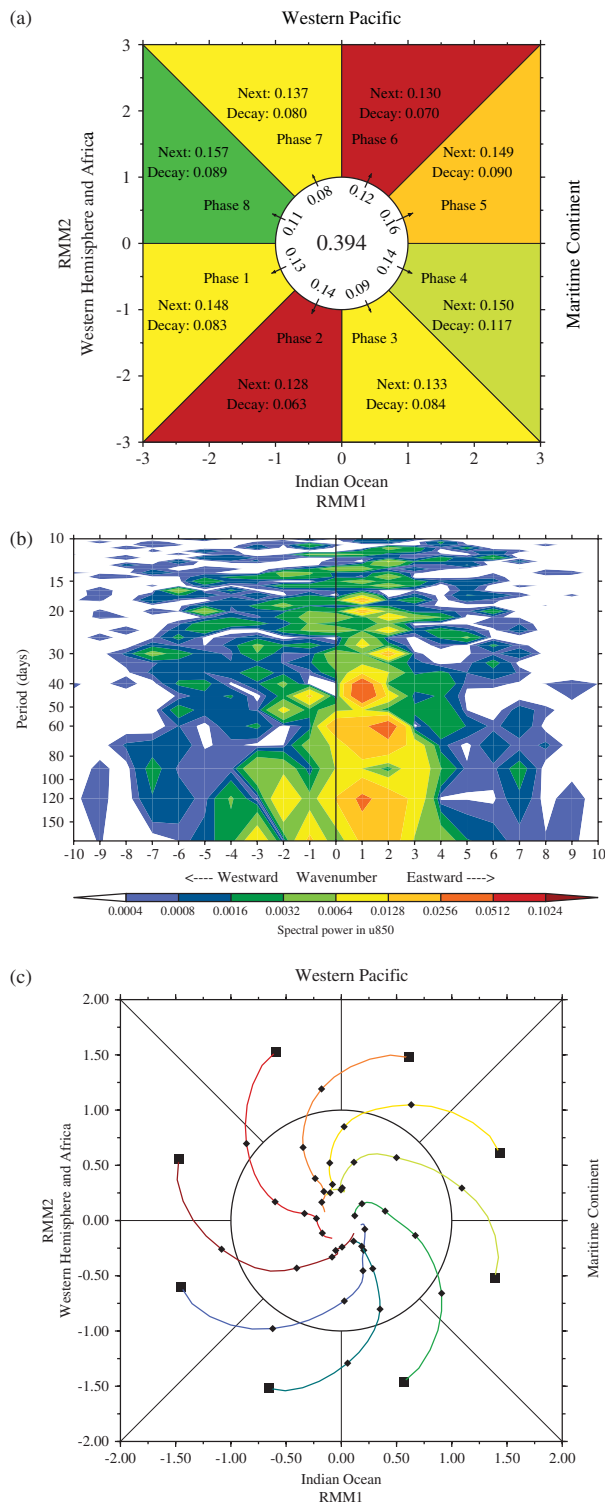
ⓒ 2013 The Authors. *Quarterly Journal of the Royal Meteorological Society*
published by John Wiley & Sons Ltd on behalf of the Royal Meteorological Society.

Q. J. R. Meteorol. Soc. (2014)

(a) Western Pacific

(b)

(c) Western Pacific

Figure 9. As in Figure 1(b), (d) and (f), but for the 1.5F-20yr simulation.

1.5F-20yr (Figure 9(b)) than in CTL-20yr (Figure 1(d)), although the period is longer than in NCEP−NCAR reanalysis (Figure 1(c)). Other diagnostics from the CLIVAR Madden−Julian Oscillation Working Group (2009), including variance in 20−100 day filtered OLR and rainfall (not shown), confirm the improvement in subseasonal convective variability in 1.5F-20yr. MJO events in 1.5F-20yr have longer lifetimes (Figure 9(c)) than in CTL-20yr (Figure 1(f)). The Maritime Continent remains a barrier to MJO propagation in 1.5F, as seen by the too-quick decay of Phase 2−4 MJO activity toward the unit circle in 1.5F-20yr relative to observations (Figure 1(e)). Propagation is substantially improved over CTL-20yr, however, in which events often decayed into the unit circle within 5 days.

Phase composites of anomalies (from the daily climatology of each model) in OLR, precipitation and winds show that 1.5F-20yr has stronger, more spatially coherent anomalies in convection than CTL-20yr (not shown). This is particularly true on the Equator: CTL-20yr often has local minima in the magnitude of OLR anomalies on the Equator, with local maxima 5−10° away from the Equator in each hemisphere. These phase composites are not included here, but are shown in Klingaman and Woolnough (2013).

6. Discussion

This study illustrates the value of using relatively low-resolution, computationally inexpensive initialized hindcasts to examine the sensitivity of tropical convection to parametrization changes. We tested 21 changes independently, plus 15 combinations of changes (section 3.1). For our primary set of four experiments (CTL, 1.5F, NoCMT and 1.5F+NoCMT), performing 30 day hindcasts instead of 20 year atmosphere-only simulations saved 70 years of model integrations. This experimental framework benefited from the agreement between the biases in the representations of the MJO in CTL-20yr and the CTL hindcasts; the phase 2 lag composite from CTL-20yr (Figure 1(f)) is strikingly similar to the CTL Day-n hindcast composite (Figure 4(a)). Had CTL demonstrated considerable skill when initialized with a strong MJO, it would have been more difficult to use the initialized-hindcast method to improve the MJO in the climate simulations. Still, the framework shows considerable promise for reducing systematic errors, not only in the mean state −for which it is most commonly used −but also in modes of variability such as the MJO.

Those familiar with hindcast experiments may be surprised at the small number of cases in this study. We analysed only 14 cases (Table 1), with only two start dates (Day-n and Day-$n+10$) and one 'ensemble member' per case. The cases were highly consistent: a strong MJO in Phase 2 followed by a strong MJO in Phase 6 at most 30 days later, with strong WH04 amplitude on all days in between. Phase 2 cases were chosen because more MJO events are generated in this phase than in any other (Figure 1(a)). The similarity among the cases generated a coherent composite, but might also have led to phase-dependent results. The Day-$n+10$ simulations were designed to test this by initializing the model with phase 3 or 4 activity, but they still rely on the same small sample of very similar MJO events. As it turned out, the results are not phase-dependent: 1.5F improved the strength, persistence and propagation of MJO activity in all phases in a 20 year simulation (Figure 9). As noted in section 5.2, the hindcasts did not test the ability of the model to generate an MJO when one was not present in the initial conditions. A more robust implementation of this framework, therefore, would select MJO events that began in each of the eight phases, initialize on many days for each case and include some cases without a strong MJO in the initial conditions. Such a design would still be more computationally efficient for evaluating parametrization changes than multidecadal simulations.

The improvement in MJO activity with 1.5F agrees with recent studies, which concluded that making parametrized convection

the fraction of days with strong MJO activity in 1.5F-20yr (60.6%) very close to observations (61.0%; Figure 1(a)). (The equivalence of these numbers is a coincidence; the increase in F was not optimized to produce this result.) The distribution of MJO activity in phase space is much less equitable in 1.5F-20yr than in observations, however, with greater activity in the western Indian Ocean (Phase 2) and West Pacific (Phase 5) and less activity near the Maritime Continent (Phases 3 and 4) and in the Western Hemisphere (Phases 7 and 8). The probability of a strong MJO 'decaying' on the next day is considerably reduced in 1.5F-20yr from CTL-20yr: depending on phase, 'decay' rates are 6−10% in observations, 6−12% in 1.5F-20yr and 12−15% in CTL-20yr. Subseasonal power in $U850$ at eastward wavenumbers 1−3 is stronger in

ⓒ 2013 The Authors. *Quarterly Journal of the Royal Meteorological Society* published by John Wiley & Sons Ltd on behalf of the Royal Meteorological Society.

Q. J. R. Meteorol. Soc. (2014)

more sensitive to environmental moisture increased subseasonal variability in tropical convection (Hannah and Maloney, 2011; Hirons *et al.*, 2012b; Benedict and Maloney, 2013). Increasing this sensitivity effectively delays the triggering of convection, allowing moisture anomalies to build for a longer period of time. In the 1.5*F* hindcasts, all precipitation rates were associated with anomalously wetter columns, relative to the zonal mean, than in CTL (Figure 8). In GA2.0, as in other models, forcing convection to prefer more-humid environments over drier ones improves the coherence of tropical convection and prolongs the suppressed phase of the MJO, producing greater instability to the east of the active phase. Along these same lines, increasing *F* in GA2.0 also reduces time-step variability in convection relative to CTL (not shown). In regions of deep convection, the lag-1 correlations of time-step precipitation are weakly negative (-0.10 to -0.30) in CTL, but are weakly positive ($0.10-0.30$) in 1.5*F*. At 1.5*F* the convective parametrization is less efficient at removing instability in a time step, which increases the probability that the parametrization will trigger on consecutive time steps, resulting in a smoother temporal profile of time-step precipitation. Combined with the results of the recent studies noted above and others (Maloney and Hartmann, 2001; Bechtold *et al.*, 2008), it appears that reducing time-step variability increases subseasonal variability, at least when *F* is the mechanism.

Not all of the impacts of higher *F* are positive, however. In 1.5*F*, convection terminates lower in the troposphere, by $50-100$ hPa on average. Fewer convective plumes reach the tropical tropopause. Reducing the mean depth of convection decreases the vertical transport of heat and momentum to upper levels, producing considerable mean cold and easterly biases near $150-200$ hPa in the 1.5*F*-20yr integration (not shown). It is worth noting here than the modified Gregory and Rowntree (1990) scheme employed in GA2.0 forces plumes to detrain completely at the level of neutral buoyancy; there is no 'overshooting'. Despite these biases, *U*200 remains representative of the upper-tropospheric flow. To confirm this, we recomputed the 1.5*F*-20yr RMM indices using 300 hPa zonal winds instead of *U*200, projecting the data on to the same Wheeler and Hendon (2004) EOFs. The correlations between the two sets of RMM indices are (0.96,0.93) for (RMM1,RMM2), indicating that the reduced termination height does not influence the results in Figure 9.

As this study focuses on the MJO in hindcast simulations, we have not analysed the impact of 1.5*F* on the tropical mean state. 1.5*F*-20yr reduces many precipitation and circulation biases from CTL-20yr, particularly in the Indian Ocean, but worsens others (not shown). Detailed analysis of the effects of increased *F* on monsoon biases in HadGEM3 can be found in Bush *et al.* (2013).

7. Summary and conclusions

A series of initialized, climate-resolution ($1.875° \times 1.25°$) hindcasts of strong MJO events were used to improve the simulation of the MJO in the Hadley Centre atmospheric model, GA2.0. In its default configuration, a 20 year GA2.0 simulation had approximately half the observed MJO activity, as measured by the fraction of days that the Wheeler and Hendon (2004) RMM amplitude was ≥ 1 (Figure 1(b)). When GA2.0 produced an MJO event, the amplitude remained ≥ 1 for fewer than 5 days on average (Figure 1(f)), compared with 10 days in observations (Figure 1(e)).

To investigate the sensitivity of the deficient MJO in GA2.0 to parametrization or model-configuration changes, 37 initialized hindcasts were performed of two strong events during the Years of Tropical Convection (YoTC). Of these, one was a control; 21 implemented a single change (section 3.1); the other 15 were combinations. Only two changes improved prediction skill over control (CTL) hindcasts: increasing by the entrainment and mixing-detrainment rates for diagnosed deep and mid-level

convection (1.5*F*) and removing the vertical transport of moment by the convective parametrization (NoCMT; Figure 2). The success of the latter suggested that the convective momentum transport (CMT) was largely responsible for the loss of the initial strong 850 hPa westerlies and 200 hPa easterlies (Figure 3). This agrees with previous studies, which have found that CMT can degrade the simulation of MJO (Inness and Gregory, 1997; Ling *et al.*, 2009). This indicated that CMT for large-scale, coherent tropical convection may need to be treated separately from that for less-organized, smaller-scale convection. Sherwood *et al.* (2013) recently presented a revised treatment diluting the momentum of a convective plume that could resolve the discrepancy between the higher entrainment rates suggested by cloud studies and the lower rates resulting from parcel-based calculations, in favour of the former.

These perturbations were then tested in a wider range of hindcast cases: all MJO events in 2000–2009 in which strong activity in RMM Phase 2 was followed by strong activity in Phase 6 at most 30 days later, while maintaining an amplitude greater than one on all days in between (Table 1). Hindcasts were initialized on the first day of strong Phase 2 activity, as well as 10 days later to test the sensitivity of the results to the initial position of the active MJO. Only 1.5*F* produced a consistent, substantial increase in MJO prediction performance, with skill for the RMM indices at 22 days –at a bivariate correlation threshold of 0.6 –against 12 days of skill for CTL (Figures 4 and 5). The NoCMT hindcasts provided only a 1–2 day improvement against CTL, with increases in lead-time-dependent correlations in the first few days and reductions after day 10, despite beneficial impacts in the YoTC cases.

Increasing *F* improved skill in all three RMM components: OLR, *U*850 and *U*200 (Figure 6). Higher *F* reduced the tendency of the CTL hindcasts to produce moderate ($4-8$ mm day^{-1}) rain rates throughout the Tropics (e.g., Figure 3(b)). By forcing convection to occur preferentially in more humid environments, the relationship between rainfall and specific-humidity anomalies more closely resembled that from TRMM observations and ERA-Interim reanalysis (Figure 8). Increasing *F* also improved the spatial coherence of convection, likely because it reduced the efficiency of the convective parametrization at removing instability, leading to a smoother temporal profile of convection. The 1.5*F* hindcasts showed greater moistening and suppressed precipitation to the east of the active MJO relative to CTL (Figure 7). This translates into an improved simulation of the suppressed phase of the MJO, producing a more unstable environment that likely encourages the active MJO in 1.5*F* to propagate east. The increased spatial and temporal coherence of deep convection in 1.5*F* was associated with a stronger dynamical response, including stronger low-level westerlies and upper-level easterlies, which improved skill in the *U*850 and *U*200 RMM components. These results are consistent with recent studies that have shown an improved representation of large-scale tropical convection when the sensitivity of the convective parametrization to moisture is increased (Hannah and Maloney, 2011; Hirons *et al.*, 2012b; Benedict and Maloney, 2013).

When 1.5*F* was implemented in a 20 year atmosphere-only simulation, MJO activity increased to near-observed levels (Figure 9(a)). The maintenance and propagation of events, while an improvment over the initial 20 year simulation, was still underestimated even at 1.5*F* (Figure 9(c)). In particular, the Maritime Continent remained a barrier to eastward propagation, with MJO activity preferentially concentrated in the Indian Ocean (Phases 2 and 3) and the West Pacific (Phases 6 and 7). Klingaman and Woolnough (2013) examine the MJO in this simulation in greater detail. Here we have shown the considerable advantages of using initialized, climate-resolution, computationally inexpensive hindcasts to understand the causes of systematic errors in representations of tropical variability in a climate model.

Acknowledgements

References

Abel SJ, Shipway BJ. 2007. A comparison of cloud-resolving model simulations of trade wind cumulus with aircraft observations taken during RICO. *Q. J. R. Meteorol. Soc.* **133**: 781–794.

Alaka G, Maloney ED. 2012. The influence of the MJO on upstream precursors to African Easterly Waves. *J. Clim.* **25**: 3219–3236.

Arribas A, Glover M, Maidens A, Peterson K, Gordon M, MacLachlan C, Graham R, Fereday D, Camp J, Scaife AA, Xavier P, Colman A, Cusack S. 2011. The GloSea4 ensemble prediction system for seasonal forecasting. *Mon. Weather Rev.* **139**: 1891–1910.

Bechtold P, Köhler M, Jung T, Doblas-Reyes F, Leutbecher M, Rodwell MJ, Vitart F, Balsamo G. 2008. Advances in simulating atmospheric variability with the ECMWF model: From synoptic to decadal timescales. *Q. J. R. Meteorol. Soc.* **137**: 553–597.

Belanger JI, Curry JA, Webster PJ. 2010. Predictability of North Atlantic tropical cyclone activity on intraseasonal time scales. *Mon. Weather Rev.* **138**: 4362–4374.

Benedict JJ, Maloney ED. 2013. Tropical intraseasonal variability in version 3 of the GFDL atmosphere model. *J. Clim.* **26**: 426–449.

Bernie DJ, Guilyardi E, Madec G, Slingo JM, Woolnough SJ, Cole J. 2008. Impact of resolving the diurnal cycle in an ocean–atmosphere GCM. Part 2: A diurnally coupled CGCM. *Clim. Dyn.* **31**: 909–925.

Bush SJ, Turner AG, Woolnough SJ, Martin G, Klingaman NP. 2013. The effect of increased convective entrainment on Asian monsoon biases in the MetUM general circulation model. *Q. J. R. Meteorol. Soc.* (In Press).

Camargo SJ, Wheeler MC, Sobel AH. 2009. Diagnosis of the MJO modulation of tropical cyclogenesis using an empirical index. *J. Atmos. Sci.* **66**: 3061–3074.

Cassou C. 2008. Intraseasonal interaction between the Madden–Julian oscillation and the North Atlantic Oscillation. *Nature* **455**: 523–527.

CLIVAR Madden–Julian Oscillation Working Group. 2009. MJO simulation diagnostics. *J. Clim.* **22**: 3006–3030.

Dee DP, Uppala SM, Simmons AJ, Berrisford P, Poli P, Kobayashi K, Andrae U, Balmaseda MA, Balsamo G, Bauer P, Bechtold P, Beljaars ACM, van de Berg L, Bidlot J, Bormann N, Delsol C, Dragani R, Fuentes M, Geer AJ, Haimberger L, Healy SB, Hersbach H, Hólm EV, Isaksen L, Kallberg P, Köhler M, Matricardi M, McNally AP, Monge-Sanz BM, Morcrette JJ, Park BK, Peubey C, de Rosnay P, Tavolato C, Thépaut JN, Vitart F. 2011. The ERA-interim reanalysis: Configuration and performance of the data assimilation system. *Q. J. R. Meteorol. Soc.* **137**: 553–597.

Del Genio AD, Chen Y, Kim Y, Mao-Sung Y. 2012. The MJO transition from shallow to deep convection in Cloudsat/CALIPSO data and GISS GCM simulations. *J. Clim.* **25**: 3755–3770.

Derbyshire SH, Maidens AV, Milton SF, Stratton RA, Willett MR. 2011. Adaptive detrainment in a convective parameterization. *Q. J. R. Meteorol. Soc.* **137**: 1856–1871.

Donlon CJ, Martin M, Stark J, Roberts-Jones J, Fielder E, Wimmer W. 2012. The Operational Sea Surface Temperature and Sea Ice Analysis (OSTIA) system. *Remote Sens. Environ.* **116**: 140–158.

Fritsch JM, Chappell CF. 1980. Numerical prediction of convectively driven mesoscale pressure systems. Part I: Convective parameterization. *J. Atmos. Sci.* **37**: 1722–1733.

Fu X, Wang B. 2004. The boreal-summer intraseasonal oscillations simulated in a hybrid coupled atmosphere–ocean model. *Mon. Weather Rev.* **132**: 2628–2649.

Gall JS, Ginis I. 2011. Experimental tropical cyclone prediction using the GFDL 25-km-resolution global atmospheric model. *Weather and Forecasting* **26**: 1008–1019.

Gottschalck J, Wheeler M, Weickmann K, Vitart F, Savage N, Lin H, Hendon H, Waliser D, Sperber K, Nakagawa M, Prestrelo C, Flatau M, Higgins W. 2010. A framework for assessing operational Madden–Julian oscillation forecasts: A CLIVAR MJO Working Group project. *Bull. Am. Meteorol. Soc.* **91**: 1247–1258.

Grant ALM, Brown AR. 1999. A similarity hypothesis for shallow-cumulus transports. *Q. J. R. Meteorol. Soc.* **125**: 1913–1936.

Gregory D, Allen S. 1991. The effect of convective downdrafts upon NWP and climate simulations. *Ninth Conference on Numerical Weather Prediction*: 122–123. American Meteorological Society: Denver, CO.

Gregory D, Rowntree PR. 1990. A mass flux convection scheme with representation of cloud ensemble characteristics and stability dependent closure. *Mon. Weather Rev.* **118**: 1483–1506.

Gregory D, Kershaw R, Inness PM. 1997. Parameterization of momentum transport by convection II: Tests in single-column and general circulation models. *Q. J. R. Meteorol. Soc.* **123**: 1153–1183.

Hannah WM, Maloney ED. 2011. The role of moisture–convection feedbacks in simulating the Madden–Julian oscillation. *J. Clim.* **24**: 2754–2770.

Hendon HH. 2000. Impact of air–sea coupling on the Madden–Julian oscillation in a general circulation model. *J. Atmos. Sci.* **57**: 3939–3952.

Hendon HH, Liebmann B. 1990. A composite study of the onset of the Australian summer monsoon. *J. Atmos. Sci.* **47**: 2227–2240.

Hewitt HT, Copsey D, Culverwell ID, Harris CM, Hill RSR, Keen AB, McLaren AJ, Hunke EC. 2011. Design and implementation of the infrastructure of HadGEM3: The next-generation Met Office climate modelling system. *Geosci. Model Dev.* **4**: 223–253.

Hirons LC, Inness P, Vitart F, Bechtold P. 2012a. Understanding advances in the simulation of intraseasonal variability in the ECMWF model. Part I: The representation of the MJO. *Q. J. R. Meteorol. Soc.* **139**: 1417–1426.

Hirons LC, Inness P, Vitart F, Bechtold P. 2012b. Understanding advances in the simulation of intraseasonal variability in the ECMWF model. Part II: The application of process-based diagnostics. *Q. J. R. Meteorol. Soc.* **139**: 1427–1444.

Holloway CE, Neelin JD. 2009. Moisture vertical structure, column water vapor and tropical deep convection. *J. Atmos. Sci.* **66**: 1665–1683.

Holloway CE, Woolnough SJ, Lister GMS. 2013. The effects of explicit versus parameterized convection on the MJO in a large-domain high-resolution tropical case study. Part I: Characterization of large-scale organization and propagation. *J. Atmos. Sci.* **70**: 1342–1369.

Inness PM, Gregory D. 1997. Aspects of the intraseasonal oscillation simulated by the Hadley Centre atmospheric model. *Clim. Dyn.* **13**: 441–458.

Inness PM, Slingo JM, Guilyardi E, Cole J. 2001. Organization of tropical convection in a GCM with varying vertical resolution: Implications for the simulation of the Madden–Julian Oscillation. *Clim. Dyn.* **17**: 777–793.

Inness PM, Slingo JM, Guilyardi E, Cole J. 2003. Simulation of the Madden–Julian oscillation in a coupled general circulation model. Part II: The role of the basic state. *J. Clim.* **17**: 365–382.

Kim D, Sperber K, Stern W, Waliser D, Kang IS, Maloney E, Wang W, Weickmann K, Benedict J, Khairoutdinov M, Lee MI, Neale R, Suarez M, Thayer-Calder K, Zhang G. 2009. Application of MJO simulation diagnostics to climate models. *J. Clim.* **22**: 6413–6436.

Kim D, Sobel AH, Del Genio AD, Chen Y, Camargo SJ, Yao MS, Kelley M, Nazarenko L. 2012. The tropical subseasonal variability simulated in the NASA GISS general circulation model. *J. Clim.* **25**: 4641–4659.

Kim D, Kug JS, Sobel AH. 2014. Propagating vs. non-propagating Madden–Julian oscillation events. *J. Clim.* **27**: 111–125.

Klingaman NP, Woolnough SJ. 2013. The role of air–sea coupling in the simulation of the Madden–Julian oscillation in the Hadley Centre model. *Q. J. R. Meteorol. Soc.*, doi:10.1002/qj.2295.

Klingaman NP, Inness PM, Weller H, Slingo JM. 2008. The importance of high-frequency sea-surface temperature variability to the intraseasonal oscillation of Indian monsoon rainfall. *J. Clim.* **21**: 6119–6140.

Klingaman NP, Woolnough SJ, Weller H, Slingo JM. 2011. The impact of finer-resolution air–sea coupling on the intraseasonal oscillation of the Indian summer monsoon. *J. Clim.* **24**: 2451–2468.

Kummerow C, Barnes W, Kozu T, Shiue J, Simpson J. 1998. The Tropical Rainfall Measuring Mission (TRMM) sensor package. *J. Atmos. Oceanic Technol.* **15**: 809–817.

Lavender SL, Matthews AJ. 2009. Respose of the West African monsoon to the Madden–Julian oscillation. *J. Clim.* **22**: 4097–4116.

Lawrence DM, Webster PJ. 2002. The boreal intraseasonal oscillation: Relationship between northward and eastward movement of convection. *J. Atmos. Sci.* **59**: 1593–1606.

Leroy A, Wheeler MC. 2008. Statistical prediction of weekly tropical cyclone activity in the Southern Hemisphere. *Mon. Weather Rev.* **136**: 3637–3654.

Lin JL, Kiladis GN, Mapes BE, Weickmann KM, Sperber KR, Lin W, Wheeler M, Shubert SD, Del Genio A, Donner LJ, Emori S, Gueremy JF, Hourdain F, Rasch PJ, Roeckner E, Scinocca JF. 2006. Tropical intraseasonal variability in 14 IPCC AR4 climate models. Part I: Convective signals. *J. Clim.* **19**: 2665–2690.

Lin H, Brunet G, Derome J. 2008. Forecast skill of Madden–Julian oscillation in two Canadian atmospheric models. *Mon. Weather Rev.* **136**: 4130–4149.

Ling J, Li C, Jia X. 2009. Impacts of cumulus momentum transport on MJO simulation. *Adv. Atmos. Sci.* **26**: 864–876.

Madden RA, Julian PR. 1971. Detection of a 40–50 day oscillation in the zonal wind in the tropical Pacific. *J. Atmos. Sci.* **28**: 702–708.

Madden RA, Julian PR. 1972. Description of global-scale circulation cells in the tropics with a 40–50 day period. *J. Atmos. Sci.* **29**: 1109–1123.

Maloney ED, Hartmann DL. 2001. The sensitivity of intraseasonal variability in the NCAR CCM3 to changes in convective parameterization. *J. Clim.* **14**: 2015–2034.

Martin GM, Milton SF, Senior CA, Brooks ME, Ineson S, Richler T, Kim J. 2010. Analysis and reduction of systematic errors through a seamless approach to modeling weather and climate. *J. Clim.* **23**: 5934−5957.

Rashid HA, Hendon HH, Wheeler MC, Alves O. 2011. Prediction of the Madden−Julian oscillation with the POAMA dynamical prediction system. *Clim. Dyn.* **36**: 649−661.

Sherwood SC, Hernández-Deckers D, Colin M. 2013. Slippery thermals and the cumulus entrainment paradox. *J. Atmos. Sci.* **70**: 2426−2442.

Slingo JM, Sperber KR, Boyle JS, Ceron JP, Dix M, Dugas B, Ebisuzaki W, Fyfe J, Gregory D, Gueremy JF, Hack J, Harzallah A, Inness P, Kitoh A, Lau WKM, McAvaney B, Madden R, Matthews A, Palmer TN, Park CK, Randall D, Renno N. 1996. Intraseasonal oscillations in 15 atmospheric general circulation models: Results from an AMIP diagnostic subproject. *Clim. Dyn.* **12**: 325−357.

Small RJ, Xie SP, Maloney ED, de Szoeke SP, Miyama T. 2011. Intraseasonal variability in the far-east Pacific: Investigation of the role of air−sea coupling in a regional coupled model. *Clim. Dyn.* **36**: 867−890.

Stratton RA, Stirling A, Derbyshire S. 2009. '*Changes and developments to convective momentum transport (CMT) parameterization based on analysis of CRM and SCM*', Technical Report 590, Forecasting R&D. Met Office: Exeter, UK.

Straub KH. 2013. MJO initiation in the Real-time Multivariate MJO index. *J. Clim.* **26**: 1130−1151.

Thayer-Calder K, Randall DA. 2009. The role of convective moistening in the Madden−Julian oscillation. *J. Atmos. Sci.* **66**: 3297−3312.

Vitart F. 2009. Impact of the Madden Julian oscillation on tropical storms and risk of landfall in the ECMWF forecast system. *Geophys. Res. Lett.* **36**: L15 802, doi:10.1029/2009GL039089.

Waliser DE, Jin K, Kang IS, Stern WF, Schubert SD, Wu MLC, Lau KM, Lee MI, Krishnamurthy V, Kitoh A, Meehl GA, Galin VY, Satyan V, Mandke SK, Wu G, Liu W, Park CK. 2003. AGCM simulations of intraseasonal monsoon variability associated with the Asian summer monsoon. *Clim. Dyn.* **21**: 423−446.

Waliser DE, Moncrieff MW, Burridge D, Fink AH, Gochis D, Goswami BN, Guan B, Harr P, Heming J, Hsu HH, Jakob C, Janiga M, Johnson R, Jones S, Knippertz P, Marengo J, Nguyen H, Pope M, Serra Y, Thorncroft C, Wheeler M, Wood R, Yuter S. 2012. The 'Year' of tropical convection (May 2008−April 2010). *Bull. Am. Meteorol. Soc.* **93**: 1189−1218.

Walters DN, Best MJ, Bushell AC, Copsey D, Edwards JM, Falloon PD, Harris CM, Lock AP, Manners JC, Morcrette CJ, Roberts MJ, Stratton RA, Webster S, Wilkinson JM, Willett MR, Boutle IA, Earnshaw PD, Hill PG, MacLachlan C, Martin GM, Moufouma-Okia W, Palmer MD, Petch JC, Rooney GG, Scaife AA, Williams KD. 2011. The Met Office Unified Model Global Atmosphere 3.0/3.1 and JULES Global Land 3.0/3.1 configurations. *Geosci. Model Dev.* **4**: 919−941.

Wheeler MC, Hendon HH. 2004. An all-season real-time multivariate MJO index: Development of an index for monitoring and prediction. *Mon. Weather Rev.* **132**: 1917−1932.

Wheeler MC, Hendon HH, Cleland S, Meinke H, Donald A. 2009. Impacts of the Madden−Julian oscillation on Australian rainfall and circulation. *J. Clim.* **22**: 1482−1498.

Wilson DR, Bushell AC, Kerr-Munslow AM, Price JD, Morcrette CJ. 2008. Pc2: A prognostic cloud fraction and condensation scheme. I: Scheme description. *Q. J. R. Meteorol. Soc.* **134**: 2093−2107.

Woolnough SJ, Vitart F, Balmaseda MA. 2007. The role of the ocean in the Madden−Julian Oscillation: Implications for MJO prediction. *Q. J. R. Meteorol. Soc.* **133**: 117−128.

Xavier PK. 2012. Intraseasonal convective moistening in CMIP3 models. *J. Clim.* **25**: 2569−2577.

Zhang C. 2005. Madden−Julian oscillation. *Rev. Geophys.* **43**: RG2003, doi: 10.1029/2004RG000 158.